Heliyon 10 (2024) e28047

Contents lists available at ScienceDirect

Heliyon

journal homepage: www.cell.com/heliyon

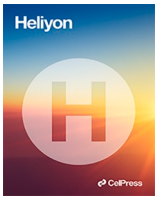

Research article

A sodium alginate - silk fibroin biosponge loaded with thrombin: Effective hemostasis and wound healing

Yansen Li [a,1], Ming Li [b,c,d,1], Chang Li [b,c,d,1], Jing Chang [b,c,d], Yuwen Hui [b,c,d], Chuanlin Wang [b,c,d,*], Wei Guo [e,**], Zhulin Li [a,***]

[a] Department of General Surgery, Beijing Chaoyang Hospital, Capital Medical University, Beijing, 100069, China
[b] Trauma Medicine Center, Peking University People's Hospital, Beijing, 100044, China
[c] Key Laboratory of Trauma and Neural Regeneration, Ministry of Education, Peking University, Beijing, 100044, China
[d] National Center for Trauma Medicine, Beijing, 100044, China
[e] Emergency Department, Peking University People's Hospital, Beijing, 100044, China

ARTICLE INFO

Keywords:
Trauma
Hemostatic method
Compound hemostatic sponge
Sodium alginate
Silk fibroin
Thrombin

ABSTRACT

In trauma first aid, rapid hemostasis is a priority, extricating patients from hemorrhagic shock and infection risks. This paper explores novel hemostatic materials, using ion-crosslinking and freeze-drying techniques. Iterative experiments determined optimal conditions for the temperature-variable mixing-freeze-drying chemical reaction of sodium alginate (SA)/silk fibroin (SF). We used SA, SA/SF, SA/SF-TB and commercial hemostatic sponge control samples to perform hemostasis experiments on rat liver injury and femoral artery injury models, and to perform wound healing experiments on rat back full-layer skin. The results showed that the hemostatic time and blood loss of SA/SF-TB group rats (liver hemorrhage model: 397.17 ± 34.80 mg, 77.83 ± 7.41 s; Femoral artery bleeding model: 940.33 ± 41.93 mg, 96.83 ± 4.07 s) was significantly better than other experimental groups, and similar to the commercial group. The wound healing experiment showed that the new granulation tissue thickness of SA/SF-TB group was thicker (380.39 ± 28.56 μm) at day 14. In addition, the material properties and biocompatibility of sponges were characterized by cell experiments and in vivo embedding experiments. All the results showed that the SA/SF-TB hemostatic sponge prepared in this study could not only seal the wound quickly and stop bleeding, but also promote the growth of epidermal cells and fibroblasts and accelerate wound healing. This new material solves the shortcomings of traditional materials such as low stability, limited shelf life, high unit price, and has good biocompatibility, easy preparation, rapid hemostasis and other excellent properties. Therefore, this innovative hemostatic material has great prospects and potential in clinical applications.

* Corresponding author. Trauma Medicine Center, Peking University People's Hospital, Beijing, 100044, China.
** Corresponding author.
*** Corresponding author.
E-mail addresses: wangchuanlinvip@163.com (C. Wang), woaiguowei111@sina.com (W. Guo), zhulin2002@163.com (Z. Li).
[1] Yansen Li, Ming Li and Chang Li contributed equally to this work.

https://doi.org/10.1016/j.heliyon.2024.e28047
Received 23 October 2023; Received in revised form 10 March 2024; Accepted 11 March 2024
Available online 15 March 2024

1. Introduction

Hemorrhage is a common and life-threatening event in trauma and surgical procedures. Rapid and effective hemostasis is crucial in reducing the risk of hemorrhagic shock. Additionally, successful wound healing substantially reduces the chances of infection in open wounds, considerably decreasing patient mortality rates [1]. Hemostasis also marks the initial phase of the wound-healing process [2]. Thus, the attainment of swift, efficient, and localized hemostasis holds crucial clinical significance in trauma and post operative recovery. The domain of materials science provides an opportunity to address this critical need, as the application of hemostatic materials can win time for trauma patients and reduce the incidence of postoperative bleeding complications. Currently, commonly used clinical hemostatic materials include hemostatic sponges [3], gels [4], powders [5], and nanofiber membranes [6]. However, these hemostatic materials possess inherent limitations, such as challenges in storage and transportation and suboptimal adhesiveness, which hinder their suitability for clinical applications. Consequently, there is an urgent demand for cost-effective, efficient, and biocompatible hemostatic materials.

We have developed a novel composite hemostatic sponge, primarily consisting of sodium alginate (SA) and silk fibroin (SF) and loaded with thrombin (TB). SA and SF each possess excellent properties, and their combination harnesses the strengths of both, making it a promising composite. As a natural wound repair material, SA exhibits excellent thickening, flocculation, and chelation properties, making it a suitable matrix for facilitating cell migration, adhesion, and regulatory functions [7]. It not only activates coagulation factor XIII to expedite the clotting process [8]but also promotes wound healing. Owing to its dual functionality, SA is extensively used in the field of biomaterials. Based on existing research, SA can also serve as a carrier with drug encapsulation and controlled release properties [9]. However, the mechanical properties of SA are not inherently stable, and during gel formation, dehydration processes may occur, diminishing its capacity for loading bioactive substances such as enzymes [10]. Research has indicated that combining the SA gel with other natural polymers can ameliorate material properties, resulting in more effective encapsulation and controlled release of bioactive substances [11]. SF, a particular natural polymer, is known to enhance the performance of SA [12]. Our designed material incorporates SF in SA, capitalizing on the inherent excellent biocompatibility and mechanical characteristics of SF [13]. SF can adsorb and concentrate essential blood components such as clotting factors and platelets, facilitating the hemostatic process [14], Additionally, it directly activates clotting factors or platelets, initiating the coagulation system [15]. Apart from its hemostatic properties, SF supports the growth of keratinocytes and fibroblasts [16], making it highly favorable for the repair and regeneration [17] of traumatic tissues, such as bone, blood vessels, nerves [18], skin, cartilage, ligaments, tendons, heart, eyes, and bladder. The complementary properties of SA-SF establish a robust theoretical foundation for our research.

SA and SF, when used independently for hemostasis, primarily function as dressings [7], and their standalone efficacy may not be highly efficient. Therefore, we incorporate TB to bolster the hemostatic effectiveness of the material. TB is a multifunctional protease that plays a pivotal role in various facets of the coagulation system of the body. It can directly interact with fibrinogen, converting it into fibrin, and concurrently activate or enhance relevant coagulation factors through protease-activated receptors (PARs) [19], leading to platelet aggregation and facilitating thrombus formation, thereby achieving hemostasis [20]. Owing to its excellent biocompatibility, high hemostatic efficacy, non-toxicity, and ready availability, TB is well suited for incorporation into hemostatic materials. For instance, in 2023, Cui et al. Investigated the use of dopamine-coated poly(caprolactone) electrospun nanofiber membranes loaded with TB for wound hemostasis [21]. However, it is worth noting that the activity of TB is considerably affected by factors such as pH and temperature [22], making its storage and transport challenging, thereby posing substantial difficulties in direct clinical application for hemostasis. Consequently, the introduction of TB into SA appropriately addresses the limited hemostatic capacity of SA and the instability of TB, allowing the unique properties of each component to be fully harnessed and maximizing the hemostatic potential of the composite material. Additionally, in our methodology, we employed Ca^{2+} cross linking, which has been demonstrated to enhance hemostasis [23]. This undoubtedly contributes to the enhanced hemostatic capabilities of our material.

In this study, we have developed an efficient hemostatic composite material using ion-crosslinking and freeze-drying techniques to combine SA, TB, and SF. This material holds the potential to expedite wound healing. We evaluated its in vitro biocompatibility through L929 cell culture, assessed its in vivo degradation by subcutaneous implantation in rats, and evaluated its in vitro coagulation ability through dynamic coagulation and adhesion experiments involving red blood cells and platelets. Additionally, we examined the in vivo hemostatic ability of the material using two rat bleeding models, involving the femoral artery and liver, and assessed its wound-healing promotion capability in a rat skin wound healing model. Our findings indicate that the material exhibits excellent physicochemical properties, including robust compressive strength, adhesion, biocompatibility, and biodegradability, as well as stable mechanical performance in vitro and in vivo. Furthermore, it demonstrates pronounced hemostatic properties both in vitro and in vivo and possesses the capacity to promote wound healing. Collectively, these qualities delineate it as a novel hemostatic sponge with substantial potential for clinical application.

2. Methods

2.1. Materials

In our study, SA was purchased from Boer Chemical Reagent Co., Ltd., Shanghai, China; SF was purchased from Suzhou Silkagen Biotech Co., Ltd., Suzhou, China; TB was purchased from HanhaiXinenzymes Bio-Tech Co., Ltd., Wuhan, China; Hematoxylin-eosin stain was purchased from Wuhan Guge Biological Technology Co., Ltd., Wuhan, China; Calcium chloride was purchased from Shanghai Aladdin Bio-Chem Technology Co., Ltd., Shanghai, China; PBS was purchased from Beijing Solarbio Technology Co., Ltd.,

Beijing, China; L929 cells were purchased from the Cell Bank of Chinese Academy of Sciences; And SD rats were purchased from Beijing Weitong Lihua Experimental Animal Technology Co., Ltd.

2.2. Preparation procedure

We added 1 g of SA powder (purchased from Boer Chemical Reagent Co., Ltd., Shanghai, China) to 10 mL of deionized water and constantly stirred the mixture at 50 °C for 20 min until the powder was completely dissolved. This resulted in a 10% SA solution, which we left to equilibrate at room temperature. We dissolved 0.2 g of SF (obtained from Suzhou Silkagen Biotech Co., Ltd., Suzhou, China) in 10 mL of deionized water to obtain a 2% SF solution. We dissolved TB (purchased from HanhaiXinenzymes Bio-Tech Co., Ltd., Wuhan, China) in deionized water (final concentration = 1 μg/mL) and set it aside.

We thoroughly mixed 10 mL of the previously prepared 10% SA solution 10 mL of deionized water and allowed the mixture stand overnight. We froze the resulting mixture at −80 °C for 12 h and then dried it in a vacuum freeze dryer for 2 days to obtain the SA sponge sample.

Similarly, we thoroughly mixed 1 mL of the 10% SA solution, 1 mL of the 2% SF solution, and 1 mL of deionized water. Subsequently, we added 1 mL of a 0.2-M calcium chloride ($CaCl_2$, purchased from Shanghai Aladdin Bio-Chem Technology Co., Ltd., Shanghai, China) solution. We freeze dried the mixture to obtain the SA–SF sponge sample (SA/SF).

We thoroughly mixed 1 mL of the 10% SA solution and 1 mL of the 2% SF solution. Subsequently, we added 1 mL of the 0.2-M $CaCl_2$ solution and then added 1 mL of the TB solution to the mixture. After ensuring adequate stirring, the mixture was freeze dried to obtain the SA–SF–TB sponge sample (SA/SF–TB).

2.3. Characterization of sponges

Following freeze drying, the hydrogel samples were immersed in liquid nitrogen and rapidly fractured to obtain cross-sectional samples. These cross-sectional samples were affixed to sample holders coated with conductive adhesive and subjected to gold sputter coating. Subsequently, the internal pore structures of the samples were observed via scanning electron microscopy (SEM; HITACHI SU8010, Japan) at an accelerating voltage of 5 kV.

The freeze-dried hydrogel samples were placed on the stage of a Fourier-transform infrared (FTIR) spectrometer (Thermo Scientific, Nicolet 6700, the USA), and a downward probe was employed to ensure close contact with the sample during measurement. The spectra were collected over 128 scans in the range of 4000–400 cm−1.

Samples, each with a height of 10 mm and a radius of 8 mm, were positioned on the operating platform of a universal testing machine (CMT6103, MTS, the USA) for evaluating the compressive properties of the hydrogels. The compression was conducted at a rate of 2 mm/min. After the measurements, the compressive modulus for three sets of samples was documented, with each set undergoing three repetitions.

The porosity of the samples was ascertained utilizing the solution volume displacement method. Initially, the dried sample was submerged in a known volume (V_1) of ethanol solution for 12 h. Subsequently, the total volume (V_2) of the ethanol solution containing the hydrogel was recorded. After sample removal, the, the remaining volume (V_3) of ethanol was measured. The porosity was calculated using the following formula:

$$\text{Porosity } (\%) = (V_1 - V_3) / (V_2 - V_3) \times 100\%$$

After freeze drying, the samples were placed on a 0.45-μm filter membrane, which in turn was positioned atop a container filled with pH 7.4 PBS buffer, allowing free passage of liquid through the membrane, thereby simulating the conditions of wound exudate. Subsequently, the swelling properties of the three hydrogels were determined. The entire system was consistently maintained at 37 °C. At predetermined time intervals (0.5, 1, 5, 10, 30, and 60 min), samples were retrieved, any residual surface moisture was removed with filter paper, and their weights were recorded. The swelling ratio was then calculated as follows:

$$\text{Swelling ratio } (\%) = (m_t - m_0) / m_0 \times 100\%$$

where m_0 denotes the initial sample weight, whereas mt corresponds to the weight of the sample at various time intervals.

2.4. In vitro biocompatibility evaluation

Samples of SA, SA/SF, and SA/SF–TB were weighed and immersed in a culture medium for 24 h to prepare extraction solutions at concentrations of 25, 50, 75, and 100 mg/mL for subsequent analyses.

The viability of cells in response to the various concentrations of extraction solutions was evaluated using the Cell Counting Kit-8 (CCK-8, Dojindo, Tokyo, Japan). In brief, L929 cells, at a density of 10^5 cells/mL, were seeded into a 96-well plate and exposed to the different concentrations of extraction solutions from each group. Following a 1-day incubation, the samples were rinsed with PBS and then incubated in a 10% CCK-8 solution (Dojindo, Tokyo, Japan). After a 2-h incubation, the absorbance of the solution was measured at 450 nm using a microplate reader (SpectraMax M2, Molecular Devices, Sunnyvale, CA, the USA).

L929 cells, at a density of 10^5 cells/mL, were seeded in a 96-well plate and subjected to a concentration of 100 mg/mL of extraction solutions from each group. After 1, 2, and 3 days of incubation, the samples underwent washing with PBS and subsequent incubation in a 10% CCK-8 solution. After 2 h of incubation, the absorbance at 450 nm was quantified using a microplate reader (SpectraMax M2,

Molecular Devices, Sunnyvale, CA, the USA).

To further evaluate cell compatibility, L929 cells were co-cultured with the 100 mg/mL extraction solutions from each group at 38 °C for 1 day. Following co-culture, the samples were cleansed with PBS and then stained with calcein-AM/propidium iodide in a dark setting for 30 min. Following a final wash, cell viability was visualized utilizing a confocal microscope (Nikon A1, Tokyo, Japan).

2.5. In vivo biocompatibility evaluation

To assess the in vivo biocompatibility and degradation of the materials, we employed pentobarbital sodium anesthesia on Sprague–Dawley (SD) rats, and their dorsal fur was removed. Following a skin incision on the dorsal surface, 20 mg of the samples were implanted. In the blank control group, skin incisions and sutures were performed without material implantation. The positive control group received filter paper implants. Skin reactions in each group were observed at 0, 3, 7, and 14 days post implantation. After 14 days, the rats from each group were euthanized, and full-thickness skin tissues were collected for hematoxylin and eosin (HE) staining to observe skin pathological changes, especially foreign-body reactions and inflammatory responses, to assess the degradation performance of the materials. Additionally, the shape and size of the heart, lung, stomach, liver, spleen, and kidney were observed in the blank control group and the SA/SF–TB group. Subsequently, HE staining was performed on these organs to evaluate whether SA/SF–TB caused substantial damage to these organs after degradation and absorption.

2.6. Dynamic coagulation assay

Fresh rat blood was drawn and mixed with anticoagulant citrate dextrose solution (comprising 20-mM citric acid, 110-mM sodium citrate, and 5-mM D-glucose) in a ratio of 9:1 (v/v) to prepare anticoagulated whole blood. Samples of SA, SA/SF, and SA/SF–TB were cut into equal-sized square pieces (0.5 cm × 0.5 cm) and placed in 5-mL centrifuge tubes. A control group without samples was also prepared. Then, 50 μL of anticoagulated whole blood was added to the surface of each sample, followed by the addition of 10 μL of the 0.2-mol/L $CaCl_2$ solution to initiate the coagulation process. The tubes were then placed in a 37 °C constant temperature oscillating incubator for 30, 60, 90, and 120s. Afterward, 3 mL of deionized water was gently added to each sample, mixed, and allowed to stand for 5 min. Finally, the absorbance of the supernatant was measured at 545 nm using a microplate reader to obtain the dynamic coagulation curves for each group. The whole blood coagulation index (BCI) was calculated using the following formula:

$$BCI = [(A_s - A_b) / (A_c - A_b)] \times 100\%$$

where A_s represents the OD value of the experimental group, A_c is the OD value of the control group, and A_b is the OD value of the blank well.

Each sample was tested in triplicate.

2.7. Red blood cell adhesion assay

SA, SA/SF, and SA/SF–TB samples were placed in a 24-well plate, and 1 mL of anticoagulated whole blood was gently added dropwise onto each sample. The 24-well plate was then incubated in a 37 °C constant temperature chamber for 5 min to allow sufficient interaction between the samples and the blood. Subsequently, deionized water was slowly added to each sample surface to wash away unbound red blood cells. The samples were then fixed with 2.5% glutaraldehyde for 12 h, sequentially dehydrated with graded alcohols, coated with gold, and then observed using SEM to examine the morphology and number of adherent red blood cells on the sample surfaces.

2.8. Platelet adhesion assay

The procedure employed for platelet adhesion was similar to that utilized for red blood cells adhesion. However, there was a difference in the initial step, where anticoagulated whole blood was centrifuged at 800 rpm for 10 min to obtain platelet-rich plasma (PRP). Subsequently, the PRP, enriched with platelets, was gently added dropwise onto the sample surfaces and incubated for 2 h. Finally, SEM was used to observe the number and activation state of adherent platelets on the sample surfaces.

2.9. In vivo hemostasis experiments

All experimental procedures used in this study were conducted in accordance with ethical guidelines and were approved by the Ethics Committee of Peking University People's Hospital (Approval Number: 2021PHE067). For this segment of the research, 30 SD rats procured from Beijing Weitong Lihua Experimental Animal Technology Co., Ltd. (License No. SCXK (JING) 2021–0011) were utilized. These animals were randomly divided into five groups, each comprising six rats: the control group, SA group, SA/SF group, SA/SF–TB group, and commercial group (using a commercially available absorbable hemostatic material, purchased from Qingdao Zhonghui Shengxi Bioengineering Co., Ltd., Qingdao, China).

Femoral Artery Hemostasis Experiment. The SD rats were anesthetized and placed in a supine position. The inner thigh was prepared by removing fur and sterilizing the area. The skin, muscle layers, and fascia were sequentially incised to expose the femoral artery. A 1-mL syringe needle was used to puncture the femoral artery, and then, each group material was placed at the puncture site.

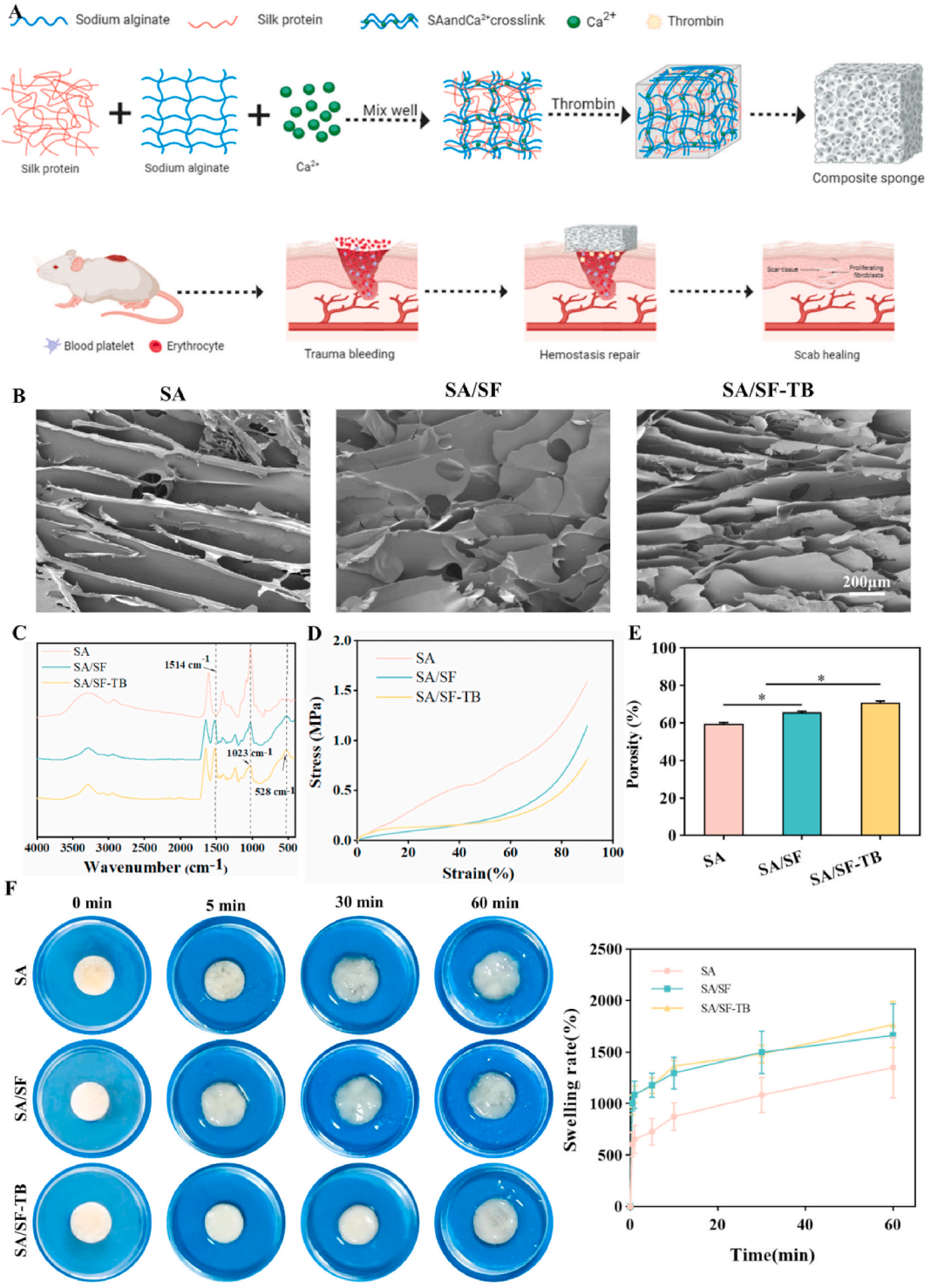

Fig. 1. (A) Schematic of the preparation process and hemostatic mechanism of the SA/SF–TB composite hemostatic sponge. (B) SEM images of the internal pore structures of SA, SA/SF, and SA/SF–TB at an acceleration voltage of 5 kV. (C) FTIR absorption spectra for SA, SA/SF, and SA/SF–TB. (D) Stress–strain curves of SA, SA/SF, and SA/SF–TB. (E) Histograms depicting the porosity of SA, SA/SF, and SA/SF–TB. (F) Photographs of SA, SA/SF, and SA/SF–TB before and after immersion in PBS buffer at pH 7.4 for 5, 10, 20, and 30 min, accompanied by the corresponding time:swelling ratio curves (**$p < 0.01$).

Adequate pressure was applied to ensure proper adhesion, and the time to complete cessation of bleeding and the volume of blood lost were recorded.

Liver Hemostasis Experiment. The SD rats were anesthetized, placed in a supine position, and their abdomen was shaved and sterilized. A midline abdominal incision, measuring approximately 5 cm in length, was made layer by layer to expose the abdominal cavity. The liver was then exposed, and a cut approximately 0.5 cm in length and 0.2 cm in depth was made on the right lobe of the liver using a surgical scalpel. Pre-prepared materials from each group were placed on the cut wound, covering and adhering to the liver tissue. Pressure was applied using a dry cotton ball above the material on the wound, and the time to complete cessation of bleeding and the volume of bleeding were recorded.

2.10. *In vivo wound-healing experiment*

A total of 24 SD rats were used for this section of the study, obtained from Beijing Weitong Lihua Experimental Animal Technology Co., Ltd. (License No. SCXK (JING) 2021–0011). The animals were randomly divided into four groups, each comprising six rats: the control group, SA group, SA/SF group, and SA/SF–TB group.

After anesthesia administration, the dorsal fur of the rats was shaved, and a circular skin defect, measuring 1 cm in diameter, was created in the middle of the dorsal region using a skin punch. For all groups except the control group, the respective composite materials were carefully applied to cover the skin defects. To document the wound-healing process, photographs of the wounds were taken on days 3, 7, and 14 post treatment. The wound-healing rate was calculated using the following formula: wound-healing rate = $(A_0 - A)/A \times 100\%$, where A_0 represents the initial wound area and A represents the current wound area.

On days 3, 7, and 14 post treatment, the rats were euthanized, and their tissues were fixed in phosphate-buffered formalin for 24 h,

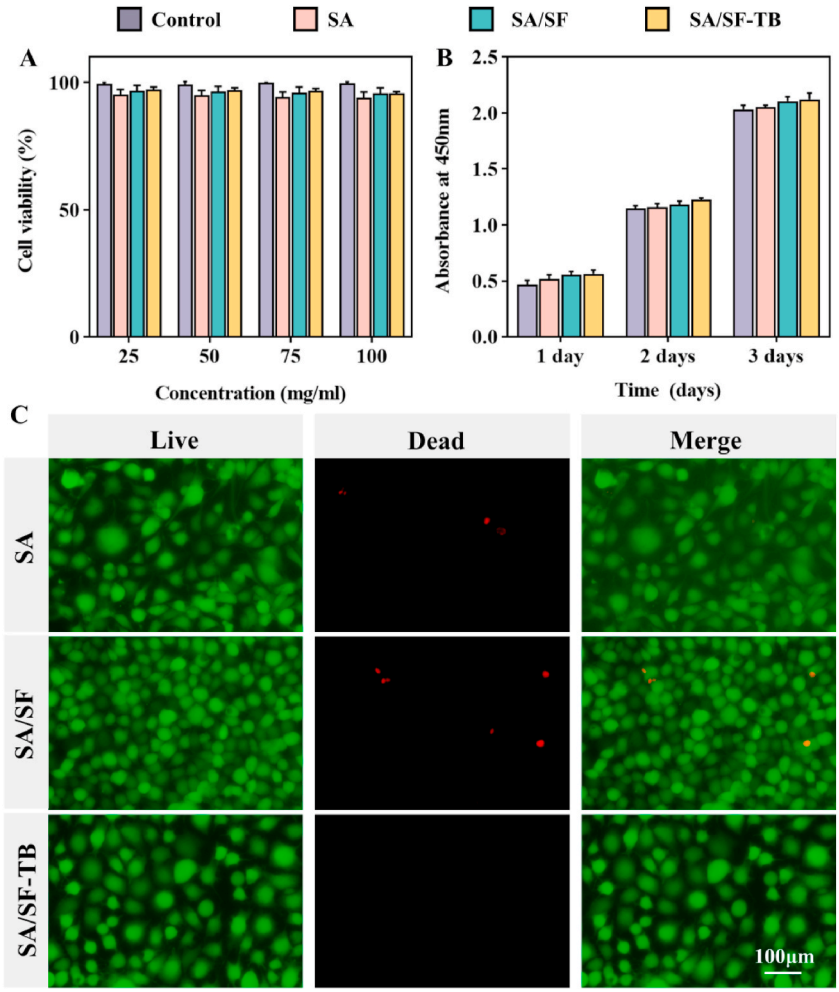

Fig. 2. (A) SA, SA/SF, and SA/SF–TB concentrations of 25, 50, 75, and 100 mg/mL extract after cultivation incubation of cell survival rate. (B) SA, SA/SF, and SA/SF–TB, each group concentration 100 mg/mL extract after cultivation incubation at 450-nm wavelength absorbance. (C) Using SA, SA/SF, SA/SF–TB, each group 100 mg/mL extract after cultivation staining confocal microscope under the obtained image.(**$p < 0.01$).

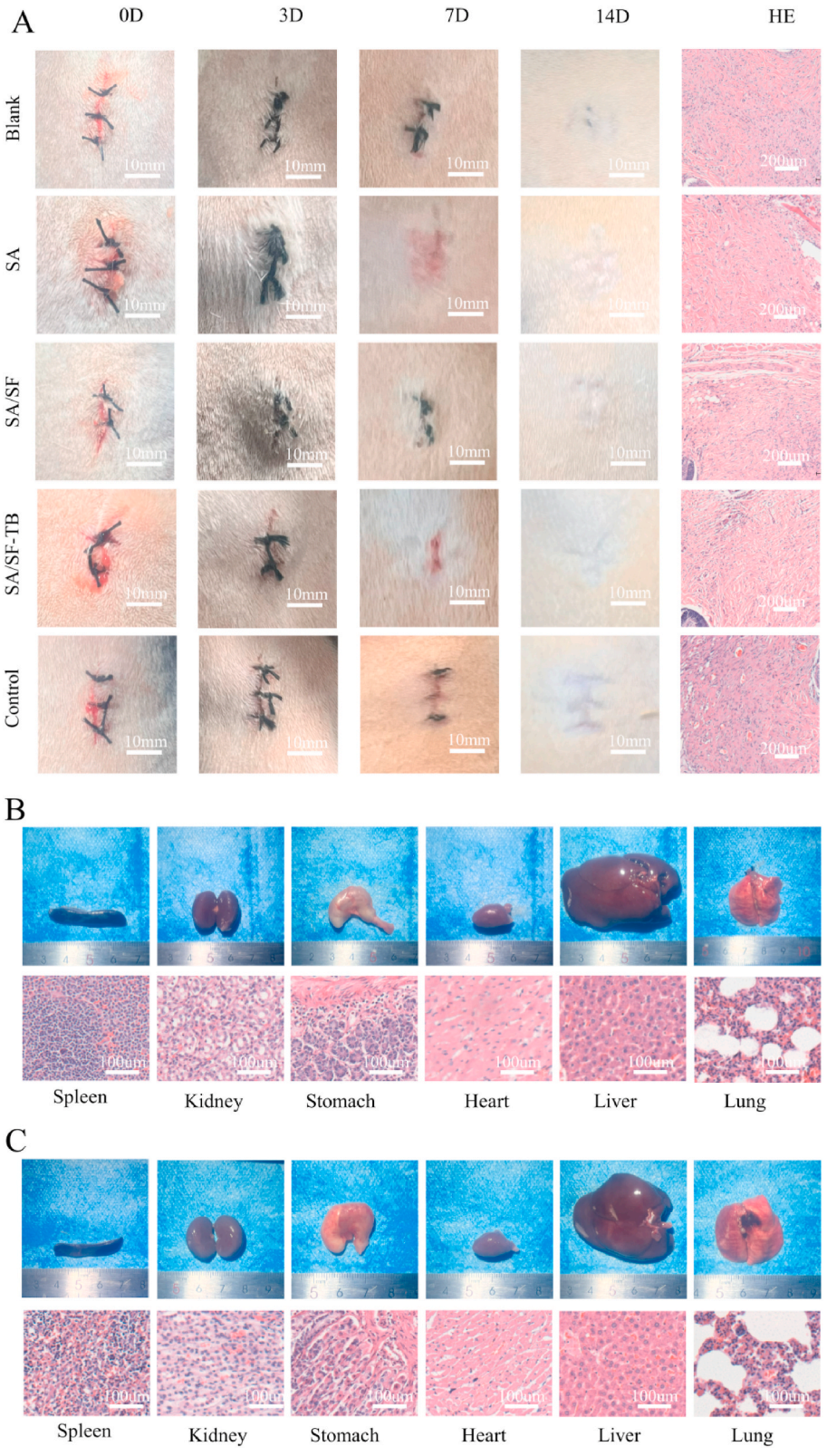

(caption on next page)

Fig. 3. (A) Photographs of SA, SA/SF, SA/SF–TB, alongside blank and control group materials taken post embedding in rat wounds at 0, 3, 7, and 14 days, and the pathological changes in tissue sections stained with HE on the 14th day after euthanizing the rats. (B) Photographs depicting the internal organs of rats in the SA/SF–TB group, accompanied by histological sections (spleen, kidney, stomach, heart, liver, and lungs). (C) Photographs showcasing the internal organs of rats in the blank group, along with histological sections (spleen, kidney, stomach, heart, liver, and lungs).

followed by dehydration and embedding in paraffin. The paraffin-embedded samples were sectioned into 5 μm slices, deparaffinized with xylene, and dehydrated using graded ethanol series. Subsequently, the sections were stained with HE according to established protocols. Histological analysis of the tissue sections was performed by a pathologist, who was blinded to the treatment groups, to assess wound healing.

2.11. Statistical analysis

All data are presented as mean ± standard deviation (SD). Statistical analyses were executed utilizing SPSS 13.0 software. To analyze the data, one-way analysis of variance was employed. The significance levels were established as: *P < 0.05, **P < 0.01, ***P < 0.001, denoting statistical significance for all executed tests. The term "ns" indicates P > 0.05, indicating no statistical difference in the results.

3. Results

3.1. Characterization of sponges

Fig. 1A illustrates the schematic representation of the preparation process and hemostatic mechanism of the SA/SF–TB composite hemostatic sponge in this study. Evaluations were conducted on the material microstructure, compressive strength, and swelling properties. SEM images of SA, SA/SF, and SA/SF–TB are presented in Fig. 1B, demonstrating that all three sponges possess uniform and smooth pore distributions. As shown in the infrared spectrum (Fig. 1C), the three materials exhibit obvious peaks near 1514, 1023, and 528 cm^{-1}. The characteristic absorption peak at 1514 cm^{-1} corresponds to the asymmetric stretching vibration of the $–NO_2$ group. Similarly, the peak at 1023 cm^{-1} is attributed to the stretching vibration of the C–O bond, while the peak at 528 cm^{-1} is associated with the out-of-plane wobble of CO_2^-. These observations confirm the consistency of functional groups across the three materials, indicating no loss of functional groups during the preparation process. Fig. 1D depicts the stress–strain curves of the three materials, revealing that SA and SA/SF–TB possess enhanced toughness and ductility compared to SA/SF. The porosity measurements depicted in Fig. 1E show that SA/SF–TB (71.54% ± 0.78%) exhibits higher porosity than SA/SF (65.44% ± 0.70%) and SA (59.52% ± 0.70%), indicating that SA/SF–TB possesses more abundant porosity, aligning better with the desired properties of hemostatic materials. Fig. 1E and F represent our assessments of the swelling properties of the three materials. Fig. 1F displays images of the materials at 0, 5, 10, 20, and 30 min post water absorption, along with the experimentally determined swelling percentages. SA/SF–TB and SA/SF show superior water absorption capabilities compared to SA at 0.5, 1, 5, and 10 min, and these results present a statistical difference. However, at 30 min and beyond, the difference was not statistically significant as all three materials reached full absorption.

3.2. In vitro safety evaluation of sponges

To assess the cellular compatibility of the materials, we employed an in vitro co-culture method with L929 cells and extracts from the three materials, followed by staining with calcein-AM/propidium iodide, as shown in Fig. 2C. This figure shows that all the three materials exhibited a high proportion of live cells, stained green by calcein-AM, whereas only a minimal number of dead cells, stained red by propidium iodide, were observed in the field of view. This indicates that the three materials demonstrate excellent cellular compatibility.

In Fig. 2A, cells were incubated in extracts with different concentrations of SA, SA/SF, and SA/SF–TB for the same duration, and the cell survival rates in each group remained elevated, showing no dependence on the extract concentration. Fig. 2B depicts cells cultured on control, SA, SA/SF, and SA/SF–TB substrates for 1, 2, and 3 days, respectively. The data revealed a progressive increase in absorbance across the 3-day span in all groups, suggesting an increase in cell numbers and suitable conditions for cell survival and proliferation. This demonstrates that none of the three materials exhibited cytotoxic effects on the cells, confirming their excellent cellular compatibility.

3.3. In vivo biosafety assessment of sponges

To assess the in vivo biocompatibility and degradation of the sample, SA, SA/SF, SA/SF–TB, and a control group (filter paper) were implanted subcutaneously in the dorsal region of rats alongside a blank control group for comparison. Skin reactions were monitored by documenting wound photos. Fig. 3A displays the wound photos at 0, 3, 7, and 14 days after subcutaneous implantation in the rats. Throughout the study, SA, SA/SF, SA/SF–TB, and the blank control group did not exhibit significant inflammatory reactions, with all wounds healing within 14 days. By contrast, the control group exhibited the formation of granulation tissue and scars, indicating suboptimal healing.

To evaluate the potential toxicity and systemic effects of the materials on other organs, the rats were euthanized after 14 days, and

gross and histological examinations were conducted on various internal organs. As shown in Fig. 3B and C, the size and morphology of organs in the SA/SF–TB group were similar to those observed in the blank control group. Microscopic analysis of the tissue sections revealed no significant differences, suggesting that SA/SF–TB did not induce strong rejection reactions or inflammation. This further demonstrates the excellent biocompatibility of SA/SF–TB.

3.4. Evaluation of in vitro blood clotting of sponges

To evaluate the coagulation capability of the materials, we conducted in vitro coagulation experiments. Fig. 4A depicts photographs of samples containing anticoagulated blood and calcium ions introduced to initiate the reaction, with images captured at 30, 60, 90, and 120 s. The images reveal that the three groups SA, SA/SF, and SA/SF–TB rapidly formed clots.

In Fig. 4B and C, the dynamic coagulation curves of the whole BCI are presented. The graphs indicate that the whole BCI of SA/SF–TB is lower than those of SA/SF and SA, implying an enhanced coagulation capability with the incorporation of SF and TB into the material. As observed via SEM (Fig. 4E), red blood cells and platelets adhere to the surfaces of all the three materials to some extent. However, the adhesion of red blood cells and platelets on SA/SF–TB is more pronounced than that on the other two materials. This observation suggests that SA/SF–TB exhibits the best coagulation performance among the three materials, demonstrating that coagulation enzymes are effectively operational within SA/SF–TB, promoting the aggregation and adhesion of activated blood cells to

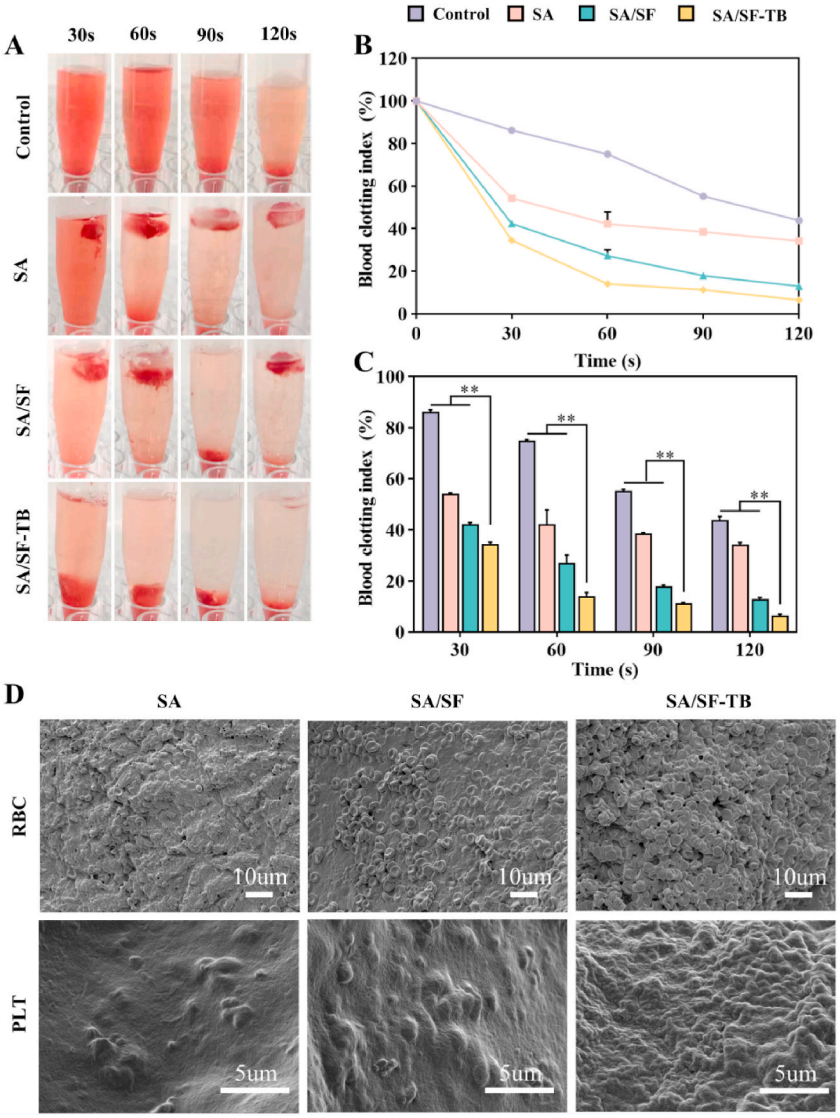

Fig. 4. (A) Photographs illustrating in vitro coagulation at 30, 60, 90, and 120 s for SA, SA/SF, SA/SF–TB, and the control group. (B) Dynamic coagulation curves depicting the whole BCI. (C) Statistical results of the whole BCI following repeated measurements. (D) SEM images of red blood cells and platelets adhered to the surfaces of SA, SA/SF, and SA/SF–TB ($n = 3$, $^{**}p < 0.01$).

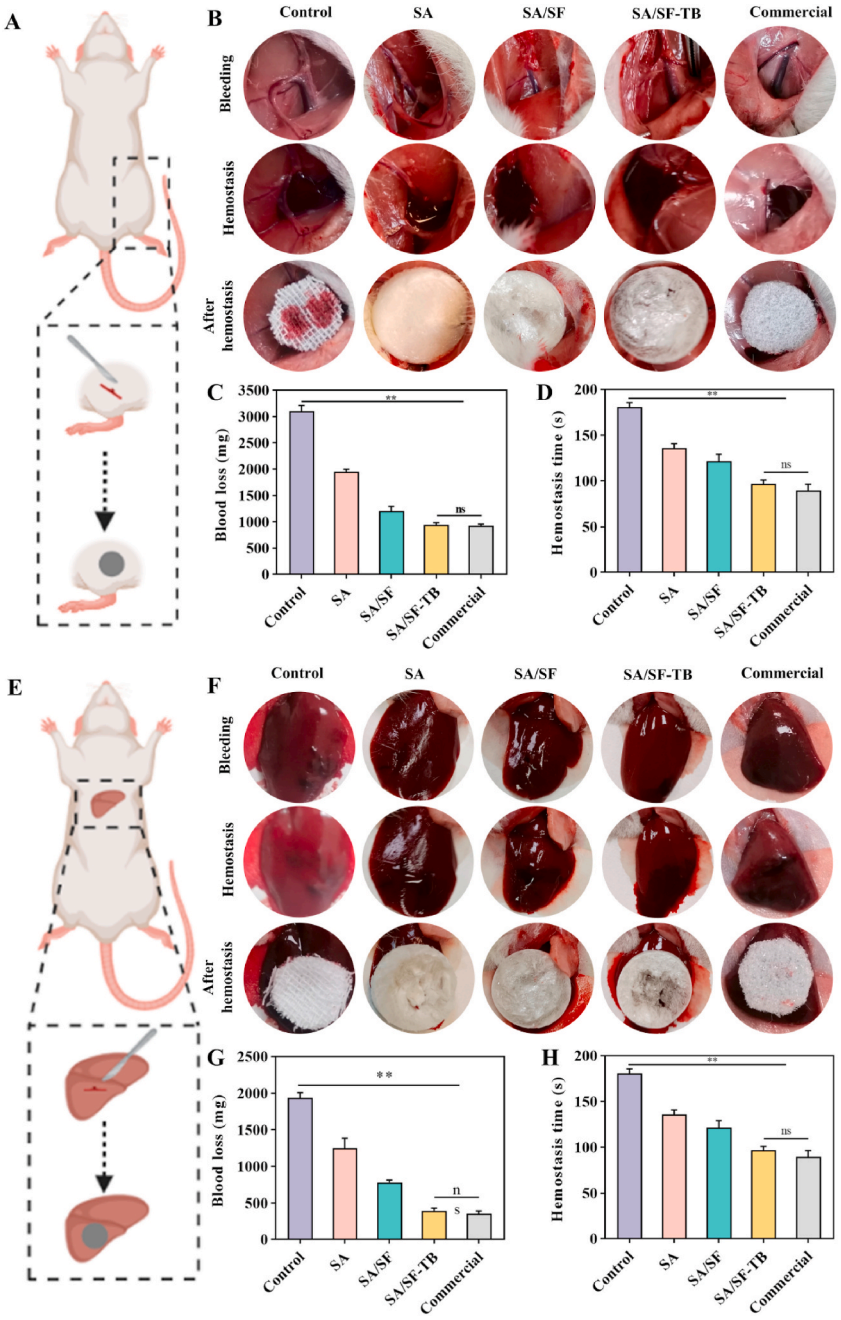

Fig. 5. (A) Schematic of the rat femoral artery hemorrhage model. (B) Sequential photographs depicting the hemostasis process in the femoral artery hemorrhage model (from left to right: control, SA, SA/SF, SA/SF–TB, and commercial groups). (C) Statistical results of blood loss in the femoral artery hemorrhage model across the control, SA, SA/SF, SA/SF–TB, and commercial groups. (D) Statistical results of hemostasis duration in the femoral artery hemorrhage model across the control, SA, SA/SF, SA/SF–TB, and commercial groups. (E) Schematic illustration of the rat liver bleeding model. (F) Sequential photographs depicting the hemostasis process in the liver bleeding model (from left to right: the control, SA, SA/SF, SA/SF–TB, and commercial hemostatic material groups). (G) Statistical results of blood loss in the liver bleeding model across the control, SA, SA/SF, SA/SF–TB, and commercial groups. (H) Statistical results of hemostasis duration in the liver bleeding model across the control, SA, SA/SF, SA/SF–TB, and commercial groups (n = 6, **p < 0.01).

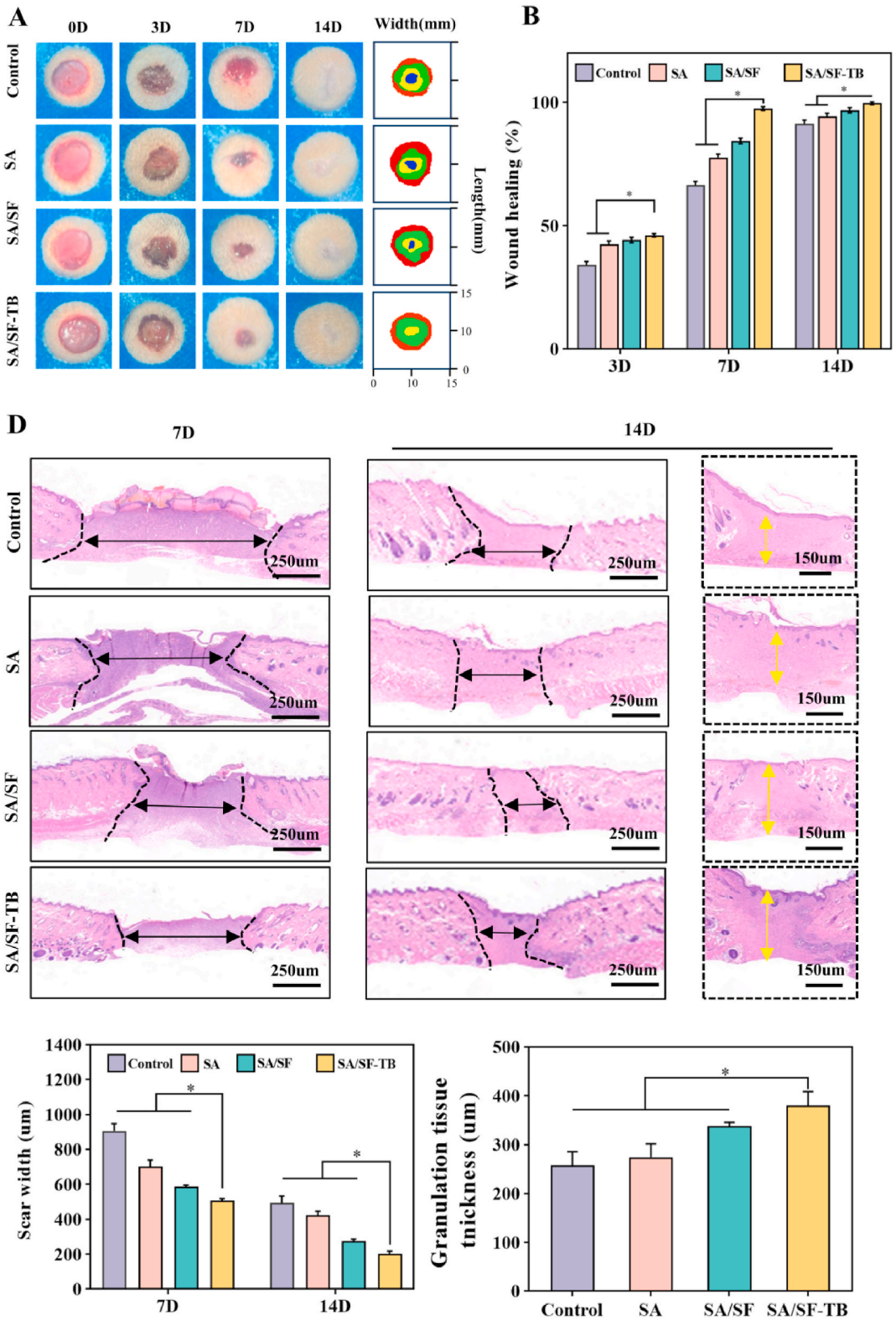

Fig. 6. (A) Photographs of the rat skin wound-healing process (from top to bottom respectively are the control, SA, SA/SF, and SA/SF–TB groups). (B) Statistical results of wound-healing rates at days 3, 7, and 14 in the skin wound-healing model of the control, SA, SA/SF, and SA/SF–TB groups. (C) Skin wound-healing model sections on days 7 and 14 for the control, SA, SA/SF, and SA/SF–TB groups. (D) Statistical results of granulation tissue thickness at days 7 and 14 in the skin wound-healing model for the control, SA, SA/SF, and SA/SF–TB groups. (n = 6, *p < 0.0001).

effectively achieve hemostasis.

3.5. Evaluation of hemostatic performance in vivo

To comprehensively evaluate the in vivo hemostatic efficacy of the materials, in vivo hemostasis experiments were performed using two rat models: the femoral artery and liver hemorrhage models. We evaluated the hemostatic capability of three hemostatic sponges in comparison with control groups (gauze) and a commercial product (absorbable hemostatic material). Fig. 5A and E illustrate the schematic diagrams of the rat models, while Fig. 5B and F shows images of the respective wounds.

In the liver bleeding model (Fig. 5B), the recorded data for blood loss and bleeding time indicate that SA/SF–TB significantly reduced blood loss (397.17 ± 34.80 mg) and shortened hemostasis time (77.83 ± 7.41 s) in contrast to SA/SF (780.83 ± 32.03 mg, 107.67 ± 8.69 s, $p < 0.0001$), SA (1247.50 ± 137.14 mg, 123.83 ± 9.11 s, $p < 0.0001$), and the control group (1937.50 ± 68.50 mg, 146.83 ± 6.27 s, $p < 0.0001$). There was no significant difference between the performance of SA/SF–TB and the commercial group (354.83 ± 37.24 mg, 70.33 ± 10.95 s, $p > 0.05$).

In the femoral artery bleeding model (Fig. 5G), the data pertaining to blood loss and bleeding duration closely aligned with the findings from the liver bleeding model. SA/SF–TB demonstrated a notably reduced blood loss (940.33 ± 41.93 mg) and a shorter time to achieve hemostasis (96.83 ± 4.07 s) compared to SA/SF (1200.83 ± 88.97 mg, 121.67 ± 7.69 s, $p < 0.0001$), SA (1950.83 ± 46.56 mg, 135.83 ± 5.12 s, $p < 0.0001$), and the control group (3103.33 ± 104.90 mg, 180.67 ± 5.05 s, $p < 0.0001$). There was almost no significant difference between SA/SF–TB and the commercial group (924.50 ± 31.86 mg, 89.83 ± 6.52 s, $p > 0.05$).

The experiments demonstrate that SA/SF–TB exhibits excellent in vivo hemostatic performance, nearly equivalent to that of clinically used hemostatic dressings. This suggests its potential application in various clinical trauma scenarios.

3.6. Evaluation of promoting tissue healing performance

To assess the wound-healing properties of the hemostatic materials, we conducted in vivo wound-healing experiments using a rat skin wound-healing model. To document the wound-healing process, photographs of the wounds were captured at days 3, 7, and 14 post treatment, as shown in Fig. 6A. It is evident that the SA/SF–TB group exhibited a high wound-healing rate, resulting in a smoother wound surface. Figure B illustrates the wound-healing rates on days 3, 7, and 14. Notably, by day 7, the wound-healing rate in the SA/SF–TB group (97.45% ± 0.78%) was significantly higher than those in the SA/SF (84.37% ± 1.11%), SA (77.72% ± 1.32%), and control groups (66.49% ± 1.50%) ($p < 0.0001$). This indicates that the SA/SF–TB group exhibited a high wound-healing efficiency, approaching complete wound closure by day 7.

Furthermore, to assess the quality of wound healing, we performed histological staining and observations, as depicted in Fig. 6C. The images reveal that the SA/SF–TB group exhibited superior wound-healing outcomes with high efficiency. Fig. 6D presents the scar width and granulation tissue thickness on days 7 and 14. The results demonstrate that by day 14, the scar width in the SA/SF–TB group (201.83 ± 15.34 μm) was smaller than those in the SA/SF (275.89 ± 9.87 μm), SA (423.52 ± 22.28 μm), and control (492.01 ± 40.57 μm) groups. Additionally, the granulation tissue thickness in the SA/SF–TB group (380.39 ± 28.56 μm) was considerably greater than those in the SA/SF (337.59 ± 8.00 μm), SA (274.59 ± 27.12 μm), and control (257.19 ± 228.38 μm) ($p < 0.0001$) group. These findings collectively suggest that SA/SF–TB is an effective wound-dressing material capable of efficiently promoting wound healing.

4. Discussion

In the process of wound-healing, efficient hemostasis is often considered the initial crucial step, making the quest for suitable hemostatic materials a notably important endeavor [24]. In this study, we have developed a novel hemostatic sponge using SA, a coagulation enzyme, and SF. These three components complement each other, working in harmony to create a portable, highly effective, readily available, biocompatible, and outstandingly hemostatic sponge. Moreover, this sponge has the added advantage of promoting wound healing. The convergence of these characteristics indeed aligns with the requirements of an ideal hemostatic material.

Currently, there are four common approaches for improving the performance of hemostatic materials [25]: the physical strategy (in which the physical structure of the material is altered to enhance water absorption for compression, concentration, and hemostasis), the biological strategy (in which biologically active substances are loaded to directly engage in the coagulation process), surface biomolecule modification (in which biologically active molecules on the material surface are used to regulate the coagulation system), and surface coating (in which material adhesion is improved to promote hemostasis through the application of surface coatings). In addition, numerous alternative methods exist for promoting hemostasis, such as employing electrical stimulation [26] to promote wound healing and hemostasis. In our study, we adopted physical and biological strategies to enhance the performance of our hemostatic material. The developed hemostatic material is a sponge comprising SA as the framework, with the incorporation of SF and a coagulation enzyme to further improve the mechanical stability and the hemostatic performance of the material. SA is a common natural material known for its high biocompatibility, ease of availability, cost-effectiveness, and ability to promote coagulation through the activation of factor XIII, making it widely applicable in various hemostatic scenarios. However, owing to its relatively weak mechanical strength, SA typically requires the addition of other materials for the enhancement of its mechanical strength. Catanzano et al. developed a composite sponge by incorporating hyaluronic acid into SA [27], and Che et al. investigated the addition of gelatin to SA [28]. Both modifications enhanced the mechanical stability and hemostatic properties of SA to varying degrees. Wei et al. discovered that soluble SF can promote platelet aggregation and adhesion to facilitate coagulation [29]. Other studies have

shown that combining SF with SA through ionic crosslinking results in a structure with greater mechanical stability. In our study, we also observed that the introduction of SF into SA improved the strength and swelling properties of SA, leading to enhanced hemostatic effectiveness compared to using SA alone. A study by Tang et al. showed that the addition of PRP to hemostatic sponges could optimize hemostatic performance, with TB playing a contributory role [30]. After optimizing the physical hemostatic performance of the novel hemostatic sponge in this study, we further introduced a coagulation enzyme to enhance the biological hemostatic performance of the material. The coagulation enzyme acts rapidly, yields significant results, and does not disrupt the coagulation mechanism, making it a commonly used hemostatic agent in clinical settings [31]. To incorporate it into our new material, we needed appropriate techniques and methods.

Ion crosslinking technology relies on the electrostatic interactions between positive and negative ions to form ion-crosslinked structures, which exhibit excellent physicochemical properties such as water absorption and extensibility [32]. In 2015, Luo et al. discovered that high-strength hydrogels could be constructed through ionic bonding [33]. In our study, we applied a small amount of calcium ions as the crosslinking agent, and the excess uncrosslinked calcium ions were removed during the synthesis process, ensuring the biogas contained only trace, safe levels of calcium. During hemostasis and wound closure, a small amount of calcium ions will be released, and studies have shown that calcium ions can act as a catalyst to accelerate the conversion rate of prothrombin to TB, thereby positively influencing the clotting process [34]. Consequently, the application of calcium ions in our study is deemed safe and beneficial. Meanwhile, freeze drying is a method of drying materials through the sublimation of ice crystals. This technique preserves the structural integrity of the material and thoroughly removes moisture, yielding a lightweight and portable product. For hemostatic sponges, freeze drying can protect the biological activity of the material against degradation. Additionally, the porous and loose structure formed by freeze drying is conducive to the full utilization of the water absorption capacity of the material. In 1999, Madihally et al. pioneered the use of freeze-drying technology to fabricate porous organic polymers [35]. These techniques, owing to their simplicity and efficiency, are well suited for enhancing the performance of hemostatic materials. In this study, we successfully prepared an SA–SF–TB sponge sample using ion-crosslinking and freeze-drying technologies, achieving good mechanical stability and swelling properties.

To further evaluate the clinical applicability of the novel hemostatic material, we corroborated its biocompatibility and safety through comprehensive in vitro and in vivo experiments. In vitro analyses involved evaluating cell viability on the material surface to explore the interaction between the material and cells. It is well documented that various physicochemical interactions occur at the interface between the material surface and bioactive substances. These interactions may be influenced by characteristics such as the size, shape, roughness, and surface coatings of materials [36]. For materials that come into contact with bioactive substances, these in vitro tests are necessary. In vivo, the study focused on determining the degradability of the material in rat tissues, mainly by evaluating the foreign-body reaction of rats to the implanted material and observing the occurrence of inflammation. The principle behind this test is that macrophages and foreign-body giant cells may trigger various foreign-body reaction events during wound healing after implantation of a foreign material. This can be observed by examining the morphological structure of proteins, cells, and other constituents to determine any potential safety concerns [37]. Based on the experimental results, the novel hemostatic material presented in this study demonstrates excellent biocompatibility in vitro and in vivo settings.

Wound healing is an essential process in hemostasis or post-injury recovery in the body. The process of wound healing can be roughly divided into four stages: hemostasis, inflammation, remodeling, and proliferation. Among these stages, hemostasis is the cornerstone of the entire cascade reaction, indicating the close and complementary relationship between hemostasis and wound healing. Therefore, in this study, we evaluated the hemostatic performance of the material from in vitro and in vivo perspectives, and we assessed the pro-healing properties of the material through in vivo experiments. The in vitro coagulation process may be characterized by factors such as the degree TB activation, the concentration of TB, and the local concentration of active cells and substances [38]. These factors are indispensable and dynamically change during physiological coagulation processes [39]. Consequently, we monitored the in vitro whole BCI through swelling rate curves, dynamic coagulation experiments, red blood cell adhesion experiments, and platelet adhesion experiments to analyze the role of the hemostatic sponge in thrombus formation. We also observed the adhesion ability of the material to red blood cells and platelets. We found that the novel material designed in this study exhibits good swelling properties, efficient coagulation, and excellent adhesion to red blood cells and platelets. Therefore, we hypothesize that the material achieves hemostasis by rapidly forming a thrombus through water absorption and expansion, followed by platelet and red blood cell recruitment. In vivo hemostasis depends on compression and adsorption properties of the material and may involve tissue adhesion properties [40], the formation of a sealed space to promote wound granulation tissue growth [41], and the promotion of skin healing [42], among other factors. To test the comprehensive in vivo hemostatic performance, we established models for skin healing, femoral artery bleeding, and liver bleeding. We found that the SA/SF–TB hemostatic material designed by our team also demonstrates excellent in vivo hemostatic performance and promotes tissue regeneration and healing.

In summary, based on the design concept of the developed material, relevant literature, and our experimental data, we propose that its outstanding hemostatic performance may be attributed to the following factors:

1. The ability of the material to absorb and swell upon contact with fluids, effectively exerts pressure conducive to hemostasis and facilitates the accumulation of red blood cells, platelets, and coagulation factors, thus promoting hemostasis. 2. The maintenance of adequate biological activity of TB within this composite material, further enhancing its intrinsic hemostatic properties. 3. The ability of the material to stimulate cell proliferation, which could contribute to limiting bleeding occurrences. However, it is crucial to augment these assertions with additional supporting data, which will be the focus of our future research endeavors.

5. Conclusion

In this study, the SA/SF-TB hemostatic sponge developed by ion crosslinking and freeze-drying technology showed rapid hemostasis and healing promotion in vivo and in vitro, and had good biosafety and degradability. The innovative material overcomes the shortcomings of traditional hemostatic materials such as low hemostatic effect, difficult preparation, preservation, transportation and high cost, and has excellent properties such as good biocompatibility, easy preparation and rapid hemostatic, which is expected to be applied in a variety of clinical occasions.

Funding

This work was supported by National Key R&D Program of China (2022YFC3006200), National Natural Science Foundation of China (82002471, 81901251, 82003992), Beijing Natural Science Foundation (7232185), and Peking University People's Hospital Scientific Research Development Funds (RDX2023-10).

Institutional review board statement

The study was conducted according to the guidelines of the Declaration of Helsinki, and approved by the Animal Ethics Committee of Peking University People's Hospital (approval number: 2021PHE067).

Data availability statement

All data that support the findings of this study are included within the article.

Disclosure of potential conflicts of interest

No potential conflicts of interest were disclosed.

CRediT authorship contribution statement

Yansen Li: Supervision, Project administration, Investigation, Conceptualization. **Ming Li:** Supervision, Project administration, Investigation, Conceptualization. **Chang Li:** Writing – original draft, Formal analysis, Data curation. **Jing Chang:** Visualization, Resources, Data curation. **Yuwen Hui:** Visualization, Validation, Data curation. **Chuanlin Wang:** Supervision, Project administration, Funding acquisition, Conceptualization. **Wei Guo:** Supervision, Project administration, Funding acquisition, Conceptualization. **Zhulin Li:** Supervision, Project administration, Funding acquisition, Conceptualization.

Declaration of competing interest

The authors declare that they have no known competing financial interests or personal relationships that could have appeared to influence the work reported in this paper.

References

[1] C. Dai, Y. Yuan, C. Liu, J. Wei, H. Hong, X. Li, X. Pan, Degradable, antibacterial silver exchanged mesoporous silica spheres for hemorrhage control, Biomaterials 30 (2009) 5364–5375.
[2] M.T. Sultan, H. Hong, O.J. Lee, O. Ajiteru, Y.J. Lee, J.S. Lee, H. Lee, S.H. Kim, C.H. Park, Silk fibroin-based biomaterials for hemostatic applications, Biomolecules 12 (2022).
[3] W. Huang, J. Wu, Z. Huang, D. Zhang, F. Chen, C. Liu, A self-gelling starch-based sponge for hemostasis, J. Mater. Chem. B 11 (2023) 1331–1343.
[4] K. Iwano, H. Toyonaga, A. Katanuma, Achieving hemostasis during endoscopic necrosectomy for walled-off pancreatic necrosis using gel immersion technique, Dig. Endosc. 34 (2022) e105–e106.
[5] J. Wang, C. Li, W. Zhang, W. Huang, Z. Liu, R. Shi, S. Wang, S. Liu, W. Shi, Y. Li, L. Xu, A contact-polymerizable hemostatic powder for rapid hemostasis, Biomater. Sci. 11 (2023) 3616–3628.
[6] D. Cui, M. Li, P. Zhang, F. Rao, W. Huang, C. Wang, W. Guo, T. Wang, Polydopamine-coated polycaprolactone electrospun nanofiber membrane loaded with thrombin for wound hemostasis, Polymers 15 (2023).
[7] A. Kumar, D.K. Sah, K. Khanna, Y. Rai, A.K. Yadav, M.S. Ansari, A.N. Bhatt, A calcium and zinc composite alginate hydrogel for pre-hospital hemostasis and wound care, Carbohydr. Polym. 299 (2023) 120186.
[8] F. Cheng, C. Liu, X. Wei, T. Yan, H. Li, J. He, Y. Huang, Preparation and characterization of 2,2,6,6-Tetramethylpiperidine-1-oxyl (TEMPO)-Oxidized cellulose nanocrystal/alginate biodegradable composite dressing for hemostasis applications, ACS Sustain. Chem. Eng. 5 (2017) 3819–3828.
[9] S. Bharati, V. Gaikwad, A. Pawar, B. Chellampillai, Investigation of a biopolymer-based pH-responsive and sustained release raft-gel-forming tablet of famotidine: in-vitro, ex-vivo, bioavailability and anti-ulcer evaluation in New Zealand albino rabbit, J. Drug Deliv. Sci. Technol. 86 (2023).
[10] P. Matricardi, C.D. Meo, T. Coviello, F. Alhaique, Recent advances and perspectives on coated alginate microspheres for modified drug delivery, Expet Opin. Drug Deliv. 5 (2008) 417–425.
[11] T. Ramdhan, S.H. Ching, S. Prakash, B. Bhandari, Physical and mechanical properties of alginate based composite gels, Trends Food Sci. Technol. 106 (2020) 150–159.
[12] Y. Wang, X. Wang, J. Shi, R. Zhu, J. Zhang, Z. Zhang, D. Ma, Y. Hou, F. Lin, J. Yang, M. Mizuno, A biomimetic silk fibroin/sodium alginate composite scaffold for soft tissue engineering, Sci. Rep. 6 (2016) 39477.

[13] L.-D. Koh, Y. Cheng, C.-P. Teng, Y.-W. Khin, X.-J. Loh, S.-Y. Tee, M. Low, E. Ye, H.-D. Yu, Y.-W. Zhang, M.-Y. Han, Structures, mechanical properties and applications of silk fibroin materials, Prog. Polym. Sci. 46 (2015) 86–110.
[14] Q. Zhang, S. Yan, M. Li, Silk fibroin based porous materials, Materials 2 (2009) 2276–2295.
[15] C. Lei, H. Zhu, J. Li, X. Feng, J. Chen, Preparation and hemostatic property of low molecular weight silk fibroin, J. Biomater. Sci. Polym. Ed. 27 (2016) 403–418.
[16] X. Zhang, M.R. Reagan, D.L. Kaplan, Electrospun silk biomaterial scaffolds for regenerative medicine, Adv. Drug Deliv. Rev. 61 (2009) 988–1006.
[17] B. Kundu, R. Rajkhowa, S.C. Kundu, X. Wang, Silk fibroin biomaterials for tissue regenerations, Adv. Drug Deliv. Rev. 65 (2013) 457–470.
[18] S. Liu, B. Liu, Q. Li, T. Zheng, B. Liu, M. Li, Z. Chen, Transplantation of fibrin-thrombin encapsulated human induced neural stem cells promotes functional recovery of spinal cord injury rats through modulation of the microenvironment, Neural Regeneration Research 19 (2024) 440–446.
[19] S.R. Coughlin, Thrombin signalling and protease-activated receptors, Nature 407 (2000) 258–264.
[20] T.K. Vu, D.T. Hung, V.I. Wheaton, S.R. Coughlin, Molecular cloning of a functional thrombin receptor reveals a novel proteolytic mechanism of receptor activation, Cell 64 (1991) 1057–1068.
[21] D. Cui, M. Li, P. Zhang, F. Rao, W. Huang, C. Wang, W. Guo, T. Wang, Polydopamine-coated polycaprolactone electrospun nanofiber membrane loaded with thrombin for wound hemostasis, Polymers 15 (2023).
[22] J.W. Fenton, M.J. Fasco, A.B. Stackrow, Human thrombins. Production, evaluation, and properties of alpha-thrombin, J. Biol. Chem. 252 (1977) 3587–3598.
[23] N. Abbasian, S.L. Millington-Burgess, S. Chabra, J.D. Malcor, M.T. Harper, Supramaximal calcium signaling triggers procoagulant platelet formation, Blood Advances 4 (2020) 154–164.
[24] P. Yu, W. Zhong, Hemostatic materials in wound care, Burns & Trauma 9 (2021).
[25] Y. Wang, W. Zhai, S. Cheng, J. Li, H. Zhang, Surface-functionalized design of blood-contacting biomaterials for preventing coagulation and promoting hemostasis, Friction 11 (2023) 1371–1394.
[26] X.Y. Zhang, J.L. Zhao, P. Xie, S.G. Wang, Biomedical applications of electrets: recent advance and future perspectives, J. Funct. Biomater. 14 (2023).
[27] O. Catanzano, V. D'Esposito, P. Formisano, J.S. Boateng, F. Quaglia, Composite alginate-hyaluronan sponges for the delivery of tranexamic acid in postextractive alveolar wounds, J. Pharmaceut. Sci. 107 (2018) 654–661.
[28] C. Che, L. Liu, X. Wang, X. Zhang, S. Luan, J. Yin, X. Li, H. Shi, Surface-adaptive and on-demand antibacterial sponge for synergistic rapid hemostasis and wound disinfection, ACS Biomater. Sci. Eng. 6 (2020) 1776–1786.
[29] W. Wei, J. Liu, Z. Peng, M. Liang, Y. Wang, X. Wang, Gellable silk fibroin-polyethylene sponge for hemostasis, Artif. Cells, Nanomed. Biotechnol. 48 (2020) 28–36.
[30] J.W. Tang, W.W. Yi, J.H. Yan, Z. Chen, H.W. Fan, D. Zaldivar-Silva, L. Agüero, S.G. Wang, Highly absorbent bio-sponge based on carboxymethyl chitosan/poly-γ-glutamic acid/platelet-rich plasma for hemostasis and wound healing, Int. J. Biol. Macromol. 247 (2023).
[31] R.N. Dong, H.L. Zhang, B.L. Guo, Emerging hemostatic materials for non-compressible hemorrhage control, Natl. Sci. Rev. 9 (2022).
[32] J.Y. Sun, X. Zhao, W.R. Illeperuma, O. Chaudhuri, K.H. Oh, D.J. Mooney, J.J. Vlassak, Z. Suo, Highly stretchable and tough hydrogels, Nature 489 (2012) 133–136.
[33] F. Luo, T.L. Sun, T. Nakajima, T. Kurokawa, Y. Zhao, K. Sato, A. Bin Ihsan, X.F. Li, H.L. Guo, J.P. Gong, Oppositely charged polyelectrolytes form tough, self-healing, and rebuildable hydrogels, Adv. Mater. 27 (2015) 2722–+.
[34] Y.Z. Zhang, Y. Xu, S.J. Zhang, Z.Y. Lu, Y. Li, B.B. Zhao, The regulation roles of Ca^{2+} in erythropoiesis: what have we learned? Exp. Hematol. 106 (2022).
[35] S.V. Madihally, H.W.T. Matthew, Porous chitosan scaffolds for tissue engineering, Biomaterials 20 (1999) 1133–1142.
[36] A.E. Nel, L. Madler, D. Velegol, T. Xia, E.M.V. Hoek, P. Somasundaran, F. Klaessig, V. Castranova, M. Thompson, Understanding biophysicochemical interactions at the nano-bio interface, Nat. Mater. 8 (2009) 543–557.
[37] J.M. Anderson, A. Rodriguez, D.T. Chang, Foreign body reaction to biomaterials, Semin. Immunol. 20 (2008) 86–100.
[38] A.S. Wolberg, Thrombin generation and fibrin clot structure, Blood Rev. 21 (2007) 131–142.
[39] S. Palta, R. Saroa, A. Palta, Overview of the coagulation system, Indian J. Anaesth. 58 (2014) 515–523.
[40] L.P. Qiao, Y.P. Liang, J.Y. Chen, Y. Huang, S.A. Alsareii, A.M. Alamri, F.A. Harraz, B.L. Guo, Antibacterial conductive self-healing hydrogel wound dressing with dual dynamic bonds promotes infected wound healing, Bioactive Materials 30 (2023) 129–141.
[41] M.J. Morykwas, L.C. Argenta, E.I. SheltonBrown, W. McGuirt, Vacuum-assisted closure: a new method for wound control and treatment: Animal studies and basic foundation, Ann. Plast. Surg. 38 (1997) 553–562.
[42] A.J. Singer, R.A.F. Clark, Mechanisms of disease - cutaneous wound healing, N. Engl. J. Med. 341 (1999) 738–746.